

1 **Declaration of Competing Interests**

2 The authors acknowledge there are no con-
3 flicts of interest recorded.

4 **A method to generate initial fault stresses for**
5 **physics-based ground motion prediction consistent with**
6 **regional seismicity**

7 **Elif Oral ^{1,2}, Jean Paul Ampuero ¹, Javier Ruiz ³, Domniki Asimaki ²**

8 ¹Université Côte d'Azur, IRD, CNRS, Observatoire de la Côte d'Azur, Géoazur, 06560 Valbonne, France

9 ²Mechanical and Civil Engineering, California Institute of Technology, Pasadena CA 91125, USA

10 ³Universidad de Chile, Departamento de Geofísica, FCFM, Santiago, Region Metropolitana, Chile

11 **Key Points:**

- 12 • We introduce a practical approximation of initial fault stresses resulting from past
13 background seismicity.
14 • Stress heterogeneity due to past seismicity leaves traceable signatures on rupture
15 and ground motion.
16 • A stratified fault medium amplifies seismic radiation at high frequencies.

Corresponding author: Elif Oral, elifo@caltech.edu

17 **Abstract**

18 Near-field ground motion is the major blind spot of seismic hazard studies, mainly be-
 19 cause of the challenges in accounting for source effects. Initial stress heterogeneity is an
 20 important component of physics-based approaches to ground motion prediction that rep-
 21 resent source effects through dynamic earthquake rupture modeling. We hypothesize that
 22 stress heterogeneity on a fault primarily originates from past background seismicity. We
 23 develop a new method to generate stochastic stress distributions as a superposition of
 24 residual stresses left by previous ruptures that are consistent with regional distributions
 25 of earthquake size and hypocentral depth. We validate our method on M_w 7 earthquake
 26 models suitable for California, by obtaining a satisfactory agreement with empirical earth-
 27 quake scaling laws and ground motion prediction equations. To avoid the excessive seis-
 28 mic radiation produced by dynamic models with abrupt arrest at preset rupture borders,
 29 we achieve spontaneous rupture arrest by incorporating a scale-dependent fracture en-
 30 ergy adjusted with fracture mechanics theory. Our analyses of rupture and ground mo-
 31 tion reveal particular signatures of the initial stress heterogeneity: rupture can locally
 32 propagate at supershear speed near the highly-stressed areas; the position of high-stress
 33 and low-stress areas due to initial stress heterogeneity determines how the peak ground
 34 motion amplitudes and polarization spatially vary along the fault, as low-stress areas slows
 35 down the rupture, decrease stress drop, and change the radiation distribution before the
 36 rupture arrest. We also find that the medium stratification amplifies the moment rate
 37 spectrum at frequencies above 2 Hz, which requires understanding the interaction be-
 38 tween site effects and rupture dynamics; therefore, we highlight the need to consider a
 39 realistic fault medium on future studies of rupture dynamics. Our approach advances
 40 our understanding of the relations between dynamic features of earthquake ruptures and
 41 the statistics of regional seismicity, and our capability to model source effects for near-
 42 field ground motion prediction studies.

43 **1 Introduction**

44 Ground motion prediction is key for earthquake engineering, but faces challenges
 45 in the vicinity of faults because of outstanding knowledge gaps in modeling earthquake
 46 rupture processes. The conventional approach in earthquake engineering is to estimate
 47 ground motion intensity measures at a certain distance from an active fault, for a future
 48 event with a given magnitude, by using empirical ground motion prediction equations
 49 (GMPEs) compiled through statistical analyses of available recordings of past earthquakes.
 50 Yet, these equations assume a lognormal distribution of ground motion estimates that
 51 is only described by a standard deviation, and do not provide any information about the
 52 physical limits. Additionally, the uncertainty of GMPEs can be high when the empir-
 53 ical data is scarce. Even in well-monitored areas, available data can be limited for large,
 54 rare, events, such as M 7+ earthquakes in California. Close to the rupture, the uncer-
 55 tainty is even higher because the strong spatial variability of source properties along a
 56 rupture — such as rupture direction, rupture speed and slip distribution — can have a
 57 large impact on ground motion, as inferred from worldwide observations (e.g., Ozacar
 58 & Beck, 2004; Courboux et al., 2013; Bao et al., 2019) and supported by theoretical
 59 and numerical studies of rupture dynamics and consequent ground motions (e.g., Ben-
 60 Menahem & Harkrider, 1964; Archuleta & Hartzell, 1981; Somerville et al., 1997; Aa-
 61 gaard et al., 2004; Dunham & Bhat, 2008). Therefore, physics-based approaches, involv-
 62 ing dynamic rupture modeling that can produce realistic variability of source properties,
 63 are a promising avenue to circumvent the data gap and to advance the predictability of
 64 near-field ground motions.

65 Dynamic rupture modeling requires setting initial fault stresses according to phys-
 66 ical assumptions and prior information, and stochastic models for the generation of ini-
 67 tial stresses have been previously proposed. Initial stress heterogeneity has been neces-
 68 sary to reproduce the ground motion recordings of past earthquakes (Ide & Takeo, 1997;

69 Andrews, 1980; Guatteri & Spudich, 2000; Nielsen & Olsen, 2000). Possible origins of
70 stress heterogeneity include the residual stresses left by past seismicity, variations in fault
71 zone pore fluid pressure and fault strength, and irregular fault geometry (Harris, 2004).
72 Here, as a starting point, we focus on the former. Considering that each earthquake per-
73 turbs stresses in the vicinity of its rupture area, and that earthquake sizes follow the Gutenberg-
74 Richter (GR) power-law distribution, Andrews (1980) reasoned that seismicity should
75 maintain a heterogeneity of crustal stresses across all length scales, and introduced the
76 concept of stochastic initial stresses in earthquake modeling (Andrews & Barall, 2011).
77 Mai & Beroza (2002) constrained the parameters of random initial stress fields using finite-
78 fault slip inversion models of past earthquakes worldwide. Recent geological and geode-
79 tic observations of surface deformation during many earthquakes further support the pos-
80 sibility of such heterogeneous distribution (e.g., Manighetti et al., 2015; Milliner et al.,
81 2015).

82 There are outstanding opportunities to advance physics-based ground motion mod-
83 eling based on stochastic initial stresses. Many studies adopt the stochastic initial stress
84 model of Andrews & Barall (2011), for rupture and ground motion analyses (e.g., Oglesby
85 & Day, 2002; Ripperger et al., 2007, 2008; Aagaard & Heaton, 2008; Mena et al., 2012;
86 Lozos et al., 2015; Andrews & Ma, 2016; Liu & Duan, 2018), for GMPE development
87 in induced seismicity areas (Bydlon et al., 2019), for tsunami modeling (e.g., Geist et al.,
88 2019). These studies show that initial stress heterogeneity has a direct effect on the main
89 characteristics of dynamic rupture and ground motion. A detailed comparison of syn-
90 thetics with GMPEs by Ripperger et al. (2008) did not reproduce spectral accelerations
91 above 1 Hz. Guatteri & Spudich (2000), setting stochastic stress heterogeneity constrained
92 by the earthquake slip database of Mai & Beroza (2002), report a good agreement be-
93 tween GMPEs and long period synthetics (> 3 s), but at shorter periods their synthet-
94 ics underestimate the GMPEs. In Baumann & Dalguer (2014) where the stress hetero-
95 geneity follows a power law similar to Andrews (1980), the fit of short period synthet-
96 ics to GMPEs is improved up to 1 Hz, but the simulated ground motions at distances
97 below 10 km underestimate the GMPEs. Andrews & Ma (2016) find a good fit of their
98 synthetics to GMPEs at 10 km distances, and highlight that the compatibility with GM-
99 PE is controlled by the amplitude of the stress heterogeneity. Indeed, sensitivity anal-
100 yses based on kinematic rupture models of Crempien & Archuleta (2018) show that a
101 larger slip correlation length increases the ground motion variability. Also in dynamic
102 rupture models, as underlined by Ripperger et al. (2008), the standard deviation of ini-
103 tial stresses substantially controls the final rupture size, slip fluctuations and rupture speed
104 variations. Their result reveals the necessity to better constrain the parameters of stochas-
105 tic stress models, in order to quantify the uncertainties associated with future earthquake
106 ground motions. Enforcing physical constraints on a purely stochastic model, on the other
107 hand, is challenging. Instead, here we consider a physics-based generation mechanism
108 for stress heterogeneity driven by past seismicity.

109 We propose a new method to approximate the heterogeneous stresses induced by
110 past seismicity, which allows us to introduce constraints based on regional seismicity data.
111 A self-consistent approach to generate heterogeneous fault stresses would be to model
112 earthquake cycles that produce realistic GR seismicity. Seismic cycle models on planar
113 faults — with uniform friction properties — generate GR seismicity when the seismo-
114 genic zone is much larger than the nucleation length, i.e., the size of the smallest fault
115 patch that can slip seismically (Barbot, 2019; Cattania, 2019). Yet, achieving such con-
116 ditions in 3D earthquake cycle simulations remains a formidable computational challenge.
117 We overcome this challenge by constructing the stress field as the sum of residual stresses
118 left by a stochastic distribution of past ruptures that is consistent with the statistical
119 properties of regional seismicity. Our work is the 3D extension of a 2D methodology that
120 was developed by Ruiz et al. (2008), which showed promise by its versatility to produce
121 enhanced high-frequency radiation.

122 In the following, we first introduce our methodology. Then, we present our main
 123 findings on the effect of the initial stress heterogeneity on rupture and ground motion
 124 in the context of M 7 earthquakes in California. Next, we discuss the current limitations
 125 and potential extensions of our method. Finally, we present the conclusions of our work.

126 2 Methodology

127 2.1 Generation of initial fault stress heterogeneity

128 Our method to generate initial stresses on a given fault suitable for dynamic rup-
 129 ture modeling is built around a target earthquake with a given magnitude. For illustra-
 130 tion purposes, our target is a M_w 7 earthquake on a generic (and idealized) vertical pla-
 131 nar strike-slip fault in southern California. An example for our conceptualization is given
 132 in Fig.1, for the seismicity of the San Jacinto fault since 1960, with each past earthquake
 133 within 10 km of the fault shown as a circular rupture. For our target model, we consider
 134 a fault with a length of 75 km and a depth of 25 km, which we discretize with sub-faults
 135 of 100 m size.

136 We first generate a set of past earthquakes that are representative of the background
 137 seismicity of the fault zone, consistently with the available regional seismicity data. We
 138 set the number of past earthquakes per magnitude such that, when adding the target
 139 earthquake, the magnitude distribution follows the GR law. The b-values in southern
 140 California lie around 1 (e.g., Hutton et al., 2010; Tormann et al., 2010; Field et al., 2014)
 141 and we set $b=0.95$ as obtained by Page & Felzer (2015) based on the instrumental data
 142 of M 4-6 earthquakes. Figure 2a shows an example of magnitude distribution for a M_w 7
 143 target event.

144 We then randomly distribute the hypocenters of the past events on a fault grid.
 145 While real seismicity is distributed over a fault zone volume (Powers & Jordan, 2010)
 146 or a fault network, we consider that heterogeneous stresses on the target fault are dom-
 147 inated by stresses induced by those past events that are located at distances to the fault
 148 shorter than or comparable to their rupture sizes, and approximate those stresses as if
 149 the past ruptures were located on the target fault. We distribute the hypocentral depths
 150 according to the empirical depth distribution developed by Hauksson & Meier (2019) based
 151 on a recent catalog of southern California. The empirical distribution is provided on depth
 152 bins of 2 km (Figure 2c). We generate random depth values by sampling this empirical
 153 distribution (Figure 2b). The lateral position of the hypocenters is set randomly accord-
 154 ing to a uniform distribution. We represent each past event by a circular crack with uni-
 155 form stress drop. The crack radius (R) is derived from the seismic moment (M_0) and
 156 an assumed stress drop ($\Delta\sigma$) by $M_0 = 16/7\Delta\sigma R^3$. We set $\Delta\sigma = 3$ MPa, the average
 157 stress drop value for active tectonic regimes such as California (Kanamori & Anderson,
 158 1975). Figure 2d shows the spatial distribution of past ruptures in the example set.

159 Next, we randomly generate an order of occurrence for the set of past earthquakes.
 160 This step introduces an additional stochastic layer in our method. Ruiz et al. (2008) con-
 161 strained the order of occurrence by forcing the hypocenter position of the next event to
 162 lie in zones of high stress, above 50% of the background stress. For simplicity, here we
 163 entirely randomize the occurrence order.

164 We then compute the cumulative stress changes induced by the past events. For
 165 each event, we compute the changes in shear stress at each point of a preset fault grid
 166 based on the circular crack approximation, following the procedure detailed in Appendix
 167 A. This procedure gives the shear stress changes normalized by a constant value of nor-
 168 mal stress. It assumes uniform values of static and dynamic friction coefficients, set here
 169 to 0.7 and 0.1, respectively. Figures 2e,f show the normalized along-strike and along-dip
 170 shear stresses, respectively, for our working example. The stress change is the lowest and
 171 most uniform inside the ruptures that occurred later in the sequence and that overlap

172 little with subsequent ruptures. Hereafter, we refer to these areas of low stress as bar-
 173 riers. The largest stress values occur around barriers. The areas with less seismicity, mostly
 174 at depth, have relatively larger stress than the barriers.

175 We generated three different realizations of stochastic stresses for this study. Model I
 176 is a reference case that we calibrate for a M_w 7 event in Section 3.1. In Model II, we drew
 177 a new random set of hypocenter locations. We set the minimum magnitude of past events
 178 as 4.75 in these two models for numerical simplicity. In Model III, we lowered it to 3.5
 179 for a sensitivity analysis and drew a new random set of hypocenter locations. The min-
 180 imum crack radius is 1.35 km in Models I and II, and 0.32 km in Model III, such that
 181 the largest node spacing of both stress generation (0.1 km) and rupture modeling (0.585 km)
 182 grids are smaller than the minimum crack size (0.64 km). The total number of earth-
 183 quakes equals 123 in Models I and II, and 1846 in Model III. Figure 3 shows the mag-
 184 nitude distribution, depth distribution, and normalized stress changes for the three mod-
 185 els. Table 1 summarizes the ranges of magnitude and rupture size of past events in each
 186 model. The depth distributions of the past events in the three models are, by design, very
 187 similar to the reference distribution (Figure 2c). The largest and smallest stress spots
 188 differ between the models, owing to their different hypocentral distributions. In addi-
 189 tion, Model III has smaller high-stress zones due to its larger number of small events that
 190 contribute extra barriers.

191 Finally, we compute absolute initial stresses, by multiplying the normalized stress
 192 changes with an assumed depth-dependent effective normal stress, as detailed in Appendix
 193 B. We adopt the effective normal stress profile of Shebalin & Narteau (2017), as shown
 194 in Figure S1, which accounts for non-hydrostatic pore fluid pressure that was discussed
 195 in Rice (1992).

196 **2.2 3D modeling of rupture and wave propagation with initial stress het-** 197 **erogeneity**

198 The heterogeneous initial stresses constructed in the previous section serve as in-
 199 put for the dynamic rupture modeling of the target event. We prepare a 3D mesh of the
 200 propagation medium containing the fault. We linearly interpolate the stress ratios from
 201 the stress-generation grid onto the dynamic rupture modeling fault grid. We assume that
 202 the fault behaviour is governed by linear slip-weakening friction.

203 We initiate the rupture in a highly stressed spot by an artificial time-weakening
 204 procedure. The hypocenter location of each model is shown in Fig. 3 and provided in
 205 Table 1. We located the hypocenter far from the fault lateral borders, with a random
 206 depth in agreement with the reference depth distribution. We enforce nucleation by a
 207 time-dependent reduction of the friction coefficient (linearly from static to dynamic) in-
 208 side a circular ring that expands from the hypocenter up to a radius of 2 km, at a con-
 209 stant speed of 3 km/s, and with a width of 300 m.

210 To devise a procedure to control the arrest of the rupture, we refer to Griffith (1921)'s
 211 criterion: rupture stops if the static energy release rate, G_0 , is smaller than the fracture
 212 energy, G_c . For a circular crack-like rupture of radius R and stress drop $\Delta\sigma$, $G_0 \propto \Delta\sigma^2 R$.
 213 In dynamic rupture models governed by fault friction, G_c is constant if the frictional prop-
 214 erties are uniform. However, G_0 increases as the rupture grows, thus it becomes increas-
 215 ingly difficult to stop the rupture. In natural fault zones, energy is dissipated not only
 216 by fault friction but also by off-fault inelastic deformation, which contributes to increase
 217 G_c . In dynamic rupture models with off-fault inelasticity, G_c increases with rupture size
 218 (Andrews, 2005; Gabriel et al., 2013), which promotes rupture arrest if it overcomes the
 219 growth of G_0 with rupture size. Here we do not explicitly model off-fault plasticity but
 220 mimic its effect on G_c by setting a spatial distribution of the slip-weakening distance D_c

221 that grows as a function of horizontal distance to the hypocenter (x) as

$$222 \quad D_c(x) = D_{c,min} + (D_{c,max} - D_{c,min})(x/L)^\beta \quad (1)$$

223 where $D_{c,min}$ and $D_{c,max}$ are lower and upper values of D_c , β is a power-law exponent
 224 that we set to 3, and L is the rupture distance at which $D_{c,max}$ is reached. In our cur-
 225 rent modeling we only consider the horizontal distance x ; incorporating the vertical com-
 226 ponent and setting a smooth transition to velocity-strengthening behaviour at depth is
 227 part of our planned future work.

228 The distance-dependent D_c helps control rupture arrest at a target distance on av-
 229 erage, but the eventual rupture path and final size of a given realization of our stochas-
 230 tic model are mainly controlled by its specific stress heterogeneity. We set the param-
 231 eters controlling the D_c distribution and the average stress drop in Model I by trial-and-
 232 error in order to satisfy empirical constraints from scaling laws and GMPEs. The rup-
 233 ture lengths of earthquakes with $M_w=7$ range from 28 to 84 km (Wells & Coppersmith,
 234 1994). Following the benchmark procedures in the SCEC Dynamic Rupture Validation
 235 project (Withers et al., 2021), we considered a GMPE developed in Next Generation Attenuation-
 236 West2 (NGA-West2; Ancheta et al., 2014). Ground motion amplitude is known to cor-
 237 relate with stress drop (e.g. Cotton et al., 2013). As a starting point, we prepare initial
 238 stresses, as detailed in Appendix B. Next, we search for D_{min} and D_{max} values that give
 239 a final rupture length consistent with scaling laws. Then, we compare the simulated ground
 240 motions to GMPEs and, if necessary, we adjust the average stress drop by re-scaling the
 241 initial stresses. We specifically change μ_b and μ_s values, while keeping the same values
 242 of μ_d and S as in Appendix A, where μ_b , μ_s and S stand for the background initial shear
 243 to normal stress ratio, static friction coefficient, and the strength excess to stress drop
 244 ratio (or strength parameter) defined by Das & Aki (1977), respectively. Since seismic
 245 moment scales with rupture area and stress drop, each time we change the stress drop
 246 to better fit the GMPEs, we also need to adjust the rupture area not to compromise the
 247 event magnitude. To do so, we tune D_{min} and D_{max} values, referring to the above-discussed
 248 balance between elastic and fracture energy. The parameter set that we determined in
 249 this procedure to get a M_w 7 event for Model I: $D_{min}=0.10556$ m, $D_{max}=0.72384$ m,
 250 $L=21$ km. For other heterogeneous models, we use the same D_c function.

251 We model 3D wave propagation with a proper resolution up to 3 Hz. We use the
 252 3D spectral element code SPECFEM3D for wave propagation and rupture dynamics (Tromp
 253 et al., 2008; Kaneko et al., 2008; Galvez et al., 2014). We set 5 GLL nodes for each spec-
 254 tral element (i.e., polynomial degree of 4). In post-processing, we Butterworth low-pass
 255 filtered all synthetics at 3 Hz. The propagation medium is vertically stratified: S-wave
 256 speed equals 760 m/s at the surface and gradually increases with depth (Figure S1), as
 257 prescribed in an ongoing SCEC community benchmark effort (Withers et al., 2021) fol-
 258 lowing (Andrews & Ma, 2016). We set a fault length of 75 km which is sufficiently large
 259 for a M 7 event to allow for a smooth arrest at fault sides, and hence avoiding any ar-
 260 tificial amplification of radiation by abrupt rupture arrest. We limited the fault depth
 261 to 18 km, consistently with the depth distribution of seismicity in California (Hauksson
 262 & Meier, 2019).

263 **3 Results**

264 **3.1 A family of plausible rupture models for California**

265 The model introduced here produces ground motions in agreement with the GMPE
 266 at periods between 0.5 and 3 s. We calculated the spectral accelerations at distances up
 267 to ~ 45 km from the surface rupture (Joyner-Boore distance), at periods of 0.5, 1, and
 268 3 s, and evaluated the orientation-independent geometric mean of horizontal response
 269 spectra, GMRotD50, defined by Boore et al. (2006). Figure 4 shows the comparison of

270 Model I synthetics with GMPEs. Considering the mean values, our synthetics are in sat-
 271 isfactory agreement with the GMPE. Additional comparisons for shorter periods (Fig.
 272 S2), show that the GMPE fit is also satisfactory at 0.4 s. The ground motion amplitude
 273 at equidistant stations can be different (Figure S3); as Ripperger et al. (2008) suggested,
 274 such intra-event variability is governed by the radiation pattern and the rupture direc-
 275 tivity. When changing the stochastic distribution of stresses, we can expect changes in
 276 these rupture details, and the ground motion amplitude at a given station, i.e., the inter-
 277 event variability. Indeed, the standard deviation of spectral accelerations at a given dis-
 278 tance can vary in Models II and III (Figures S4 and S5). Ripperger et al. (2008) sug-
 279 gest that the inter-event variability is mainly controlled by the hypocenter-station con-
 280 figuration rather than the changes in stress heterogeneity. Here rupture is bilateral and
 281 the hypocenter-station configuration is similar for our three heterogeneous models. The
 282 differences between the three models are slight and mostly visible below 10 km Joyner-
 283 Boore distance for 3 s period; the decay trend with respect to GMPE remains compa-
 284 rable.

285 By generating several stochastic realizations of the spatial distribution of past seis-
 286 micity, we generate a set of earthquakes that are consistent with the regional statistics.
 287 After calibrating Model I, we kept the parameters controlling the distribution of D_c the
 288 same in Models II and III. Figure 5 shows the evolution of slip in the three models. The
 289 rupture path and slip are strongly controlled by the locations of barriers and high-stress
 290 areas. We summarized the resulting magnitude, stress drop, and surface rupture length
 291 in Table 2. In Model II, the surface rupture length is slightly larger than in Model I, and
 292 the average stress drop is the same, 2.7 MPa, such that the resulting magnitude equals
 293 7.05. In Model III, the rupture area and the average stress drop, 2.9 MPa, are larger,
 294 yielding a magnitude of 7.12. We verified that surface rupture lengths in each model are
 295 coherent with the empirical values documented by Wells & Coppersmith (1994). In sum-
 296 mary, the source properties of the three models, generated with a single set of param-
 297 eter values, are consistent with the empirical expectations about source scaling.

298 The source spectra (the Fourier amplitude of the moment-rate function) of the three
 299 models have a similar shape (Figure 6). All models exhibit high-frequency radiation in-
 300 duced by stress heterogeneity. Details of the rupture evolution in the three models are
 301 shown in supplementary figures: the evolution of slip rate in Figure S6, and the spatial
 302 distribution of peak slip velocity in Figures S7-S9. In particular, below ~ 1 Hz, Model I
 303 is closer to the ω^{-2} model (Aki, 1967; Brune, 1970). We calculated the double corner
 304 frequencies as a function of M_w after Ji & Archuleta (2021). We set the corner frequency
 305 of the ω^{-2} model as the geometric mean of the double corner frequencies. On the other
 306 hand, we see a significant amplification with respect to the ω^{-2} model above 2 Hz in all
 307 the models. We show in the Discussions section that this amplification is partially caused
 308 by the stratified medium.

309 The spatial spectra of our slip and initial stress distributions are within the expecta-
 310 tions of previous studies. Mai & Beroza (2002) showed that the spatial spectra of earth-
 311 quake slip inferred by finite source inversion can be approximated by Von Karman cor-
 312 relation functions. Following their approach, we fitted a Von Karman function to the Fourier
 313 spectra of slip of our three models. We obtained values of correlation length and Hurst
 314 exponent that are consistent with the values reported by Mai & Beroza (2002) for M 7
 315 events (Figures S10-S12). Regarding the 2D Fourier spectrum of initial stresses, Andrews
 316 (1980) suggests a spectrum decay following a power law, with exponent $\nu < 1$. Given
 317 the linear relationship between slip gradients and stress implied by elasticity, the expo-
 318 nent of slip spectrum is $< \nu + 1$, hence < 2 . Later, Lavallée & Archuleta (2003) cal-
 319 culate these values for a set of past earthquakes and report $0.78 \leq \nu \leq 1.71$. In our
 320 models, the exponent of slip and initial stress spectra follow a power law with approx-
 321 imate exponents of 0.7 and 1.7, respectively (Fig. S13), and therefore agrees with the
 322 previous studies. Moreover, Lavallée et al. (2006) evaluate the probability density func-

323 tion of slip in a set of past earthquakes and conclude that a non-Gaussian distribution
 324 better represents the observations, as opposed to the Gaussian distribution assumed in
 325 Andrews (1980). Here we found that the slip and initial stress distributions of our mod-
 326 els are both non-Gaussian (provided in Fig. S14). The decay of initial stress distribu-
 327 tion is smoother and has partial increase because of local stress concentrations, differ-
 328 ently than a Gaussian distribution. A non-Gaussian function, such as Levy or Cauchy,
 329 works better for our models, as concluded in Lavallée & Archuleta (2003).

330 **3.2 Local supershear at initially high stress patches**

331 Initial stress heterogeneity causes variations in rupture speed, including supershear
 332 speeds. Figure 7 (middle) shows the spatial distribution of rupture speed in Model I. The
 333 rupture front accelerates in areas of high initial stress, such as the deeper parts with fewer
 334 barriers, and in barrier edges, and can reach supershear speeds. Yet, the resulting su-
 335 pershear ruptures are not sustained but transient. The average speed is $0.6 V_s$, similar
 336 to the pseudo-dynamic models by Mena et al. (2012) that concluded the possibility of
 337 a local supershear because of stress heterogeneity. We obtain similar results in the other
 338 two models (Figures S15 and S16).

339 **3.3 Spatial variability of ground motion amplitude and polarization**

340 The spatial variability of ground motion amplitude is sensitive to the initial stress
 341 heterogeneity. We analyzed the peak ground velocity (PGV) in our models (Figure 8b
 342 for Model I) and in an additional homogeneous stress model (detailed in Supplemental
 343 Material) (Figure 8a). In the latter, the magnitude is M_w 7, the surface rupture extends
 344 between -20 and 20 km along strike, and the largest PGV values lie along the surface
 345 rupture. At an approximate epicentral distance of 7 km, rupture accelerates due to free-
 346 surface effects (Figures S17 and S18) and radiates waves carrying large amplitudes to
 347 further off-fault distances. Upon rupture arrest at abrupt barriers, additional fronts pro-
 348 duce large-amplitude ground motion at stations ahead of the two rupture directions. In
 349 the heterogeneous Model I, the spatial distribution of PGV is also heterogeneous and
 350 the largest values, exceeding 1 m/s, reach distances up to ~ 4 km perpendicular to the
 351 fault. Such largest PGV areas are associated with the rupture segment in between the
 352 two largest barriers (Figure 7). Differently from the homogeneous model, the fronts car-
 353 rying large PGV to farther off-fault distances start close to barriers distributed all along
 354 the rupture, instead of the fault ends. In Ripperger et al. (2008), the areas perpendic-
 355 ular to the fault plane and rupture direction in the band inside $x=[-20,20]$ km are found
 356 to be unaffected by directivity and exhibit most the inter-event differences in ground mo-
 357 tion caused by stress heterogeneity. Indeed, here we can associate the changes in peak
 358 ground motion amplitudes with the event-specific stress heterogeneity. A different het-
 359 erogeneous stress distribution (Models II and III) changes the PGV distribution, and in
 360 particular the location of the largest PGV values near the fault (shown in Figures S15
 361 and S16), similar to the results by Oglesby & Day (2002) and Ripperger et al. (2008).

362 The orientation of the maximum amplitude of ground velocity, both in the near
 363 and far field, can change because of initial stress heterogeneity. Figures 8c,d show the
 364 spatial distribution of the peak ground motion polarization for homogeneous and het-
 365 erogeneous models. Near the epicenter, the polarization is in the fault-parallel direction
 366 at stations that are located perpendicular to fault strike in both models. In the homo-
 367 geneous model, the polarization switches to fault-normal direction where the slip rate
 368 increases upon surface rupture after 3 s (Fig. S18) as indicated by arrows in Fig. 8a. In
 369 the heterogeneous model, we notice a similar transition from fault-parallel to fault-normal
 370 component. The fault-normal polarization zone is larger in the heterogeneous case, and
 371 the difference between the two cases persists to Joyner-Boore distances larger than 20 km.
 372 The pattern of PGV polarization is event-specific, depending on the spatial distribution
 373 of barriers, supporting the findings of Oglesby & Day (2002).

374 **4 Discussion**

375 One limitation of our current study is the lack of unilateral ruptures and additional
376 source complexities. Rupture is bilateral and the hypocenter depth is comparable (5-7
377 km) in our models. Verification of our results for different hypocenter locations is one
378 of the primary perspectives. To focus on initial stress heterogeneity, we also excluded
379 other potential factors such as multi-segmented faults, fault roughness, presence of fault-
380 damage zones, and non-uniform frictional properties. Understanding how the coupling
381 of these additional factors impact the rupture process and ground motions requires fur-
382 ther research.

383 To guide future studies that require generating a large set of earthquakes of a given
384 magnitude, we performed a sensitivity analysis by changing various features of the model
385 settings: hypocenter location, L parameter in equation 1, strength parameter S , and the
386 order of occurrence of past events. The resulting magnitudes range from 6.9 to 7.3. Only
387 for the case of a larger S value, rupture fails to propagate upon nucleation (Figs. S19-
388 S24). A more systematic study is warranted to evaluate the model performance within
389 a comprehensive set of rupture models considering the above factors.

390 Medium stratification amplifies high-frequency radiation and ground motion; a bet-
391 ter description of the propagation medium in terms of site geometry and stratification
392 can help to constrain high-frequency radiation. Our heterogeneous models generate en-
393 hanced high-frequency radiation, but compared to ω^{-2} decay, all models have larger spec-
394 tral amplitudes above 2 Hz. To better understand the possible origins of such excessive
395 high-frequency radiation, besides the stress heterogeneity, we created two homogeneous
396 stress cases that only differ by the presence of medium stratification. Comparing their
397 spectra (Figure 9), we identified that medium stratification alone can amplify the source
398 spectrum at high frequencies, by more than a factor of 10, and consequent ground mo-
399 tions (Figures S25 and S26). The model with stratification exceeds the estimations of
400 the empirical models ω^{-2} and Ji & Archuleta (2021) particularly above 2 Hz. Our ad-
401 ditional analyses (Figures S27-S30) show that the peak slip rate in the stratified model
402 is larger than in the homogeneous model, and such relative amplification increases to-
403 wards the surface, up to a factor of 10 at the surface. Despite the weaker rigidity in the
404 stratified model, the increase in slip rate at shallow depths amplifies the moment rate
405 above 2 Hz. To clarify whether we can improve the synthetic source spectra with respect
406 to the references when using a realistic medium, without compromising the GMPE fit,
407 we note the necessity to consider a realistic fault zone and wave propagation medium.
408 The effect of crustal velocity structure on dynamic rupture and source properties is in-
409 creasingly recognized (e.g., Prada et al., 2021; Huang, 2021). This effect is exacerbated
410 in our examples, because we did not include the competing effects of cohesion and fric-
411 tional strengthening at shallow depth. For southern California, subsurface velocity mod-
412 els are available (SCEDC, 2013), as well as recent refined models for the Ridgecrest area
413 as those derived from dense array data by White et al. (2021) and from distributed acous-
414 tic sensing data by Yang et al. (2022). Our planned future work includes the assessment
415 of the impact of medium heterogeneity on rupture dynamics and seismic radiation in south-
416 ern California.

417 A natural extension of our work is to study the effect of low velocity, damaged fault
418 zones on rupture speed. Damaged fault zones can facilitate sustained supershear rup-
419 tures (Huang et al., 2016; Oral et al., 2020). California is one of the regions where such
420 damage zones are well documented (e.g., Cochran et al., 2009; Lewis & Ben-Zion, 2010).
421 Very recently, co-seismic and pre-seismic damage zones with notable along-strike and off-
422 fault variability were identified on the fault system that hosted the 2019 M 7.1 Ridge-
423 crest earthquake (Qiu et al., 2021; Rodriguez Padilla et al., 2022). Accounting for the
424 documented damage zones in California, a primary question to address in a future study
425 is whether the local transitions of speed due to initial stress heterogeneity can evolve to
426 sustained supershear ruptures.

427 Applying our method to other regions with different Gutenberg-Richter b-values
 428 or seismotectonic settings, as a further verification of the applicability of our method,
 429 is another perspective. We focused on M_w 7 strike-slip earthquakes in California and ob-
 430 tained promising results constrained by properties of the regional seismicity. Extending
 431 our study to other regions with the available data of ground motion and past seismic-
 432 ity stands as a further test to validate the applicability of our method.

433 5 Conclusions

434 We develop a new method to generate heterogeneous initial fault stresses for dy-
 435 namic rupture modeling consistent with statistical properties of regional seismicity. Our
 436 modeling gives promising results for M_w 7-7.1 strike-slip earthquakes in California, pro-
 437 ducing ground motions and rupture characteristics consistent with empirical relations.

438 We determined certain signatures of the initial stress heterogeneity on the rupture
 439 process and consequent ground motion. Variations in rupture speed can locally reach
 440 supershear speed, where the stress is relatively large, around barriers or in areas with
 441 less barriers. The largest peak ground motion amplitudes expand to larger distance from
 442 the fault than in a homogeneous stress model. The spatial patterns of PGV amplitude
 443 and polarization are sensitive to the location of stress barriers, and hence event-specific.

444 We also find a feedback between site effects and source effects: the medium strat-
 445 ification can amplify the source spectrum at high frequencies (above 2 Hz). To better
 446 understand the medium effect on rupture and consequent ground motion, we suggest for
 447 future dynamic rupture studies to adopt realistic descriptions of the propagation medium.

448 6 Data and resources

449 SPECFEM3D is available at [https://github.com/geodynamics/specfem3d/tree/](https://github.com/geodynamics/specfem3d/tree/devel)
 450 `devel`. The modifications that we made can be found <https://github.com/elifo/specfem3d>
 451 upon the publication of our manuscript. The supplemental material includes one sec-
 452 tion of homogeneous models and thirty figures.

453 Acknowledgments

454 This work has been supported by the French government, through the UCAJEDI Invest-
 455 ments in the Future project managed by the National Research Agency (ANR) with the
 456 reference number ANR-15-IDEX-01, Southern California Earthquake Center award 21010,
 457 and the California Institute of Technology. The computations presented here were con-
 458 ducted in the Thera cluster of Geoazur, and the Resnick High Performance Computing
 459 Center, a facility supported by Resnick Sustainability Institute at the California Insti-
 460 tute of Technology. We acknowledge Caroline Ramel for IT support, and SCEC DRV
 461 benchmark participants and Yihe Huang for valuable discussions.

462 References

- 463 Aagaard, B. T., Hall, J. F., & Heaton, T. H. (2004). Effects of fault dip and slip
 464 rake angles on near-source ground motions: Why rupture directivity was minimal
 465 in the 1999 Chi-Chi, Taiwan, earthquake. *Bulletin of the Seismological Society of*
 466 *America*, *94*(1), 155–170.
- 467 Aagaard, B. T., & Heaton, T. (2008). Constraining fault constitutive behavior
 468 with slip and stress heterogeneity. *Journal of Geophysical Research: Solid Earth*,
 469 *113*(B4).
- 470 Aki, K. (1967). Scaling law of earthquake spectrum. *J. Geophys. Res.*, *72*, 1217–
 471 1231.

- 472 Ancheta, T. D., Darragh, R. B., Stewart, J. P., Seyhan, E., Silva, W. J., Chiou,
473 B. S.-J., ... others (2014). NGA-West2 database. *Earthquake Spectra*, *30*(3),
474 989–1005.
- 475 Andrews, D. J. (1980). A stochastic fault model: 1. Static case. *Journal of Geophys-*
476 *ical Research: Solid Earth*, *85*(B7), 3867–3877.
- 477 Andrews, D. J. (2005). Rupture dynamics with energy loss outside the slip zone.
478 *Journal of Geophysical Research: Solid Earth*, *110*(B1).
- 479 Andrews, D. J., & Barall, M. (2011). Specifying initial stress for dynamic heteroge-
480 neous earthquake source models. *Bulletin of the Seismological Society of America*,
481 *101*(5), 2408–2417.
- 482 Andrews, D. J., & Ma, S. (2016). Validating a dynamic earthquake model to pro-
483 duce realistic ground motion. *Bulletin of the Seismological Society of America*,
484 *106*(2), 665–672.
- 485 Archuleta, R. J., & Hartzell, S. H. (1981). Effects of fault finiteness on near-source
486 ground motion. *Bulletin of the Seismological Society of America*, *71*(4), 939–957.
- 487 Bao, H., Ampuero, J.-P., Meng, L., Fielding, E. J., Liang, C., Milliner, C. W., ...
488 Huang, H. (2019). Early and persistent supershear rupture of the 2018 magnitude
489 7.5 Palu earthquake. *Nature Geoscience*, *12*(3), 200–205.
- 490 Barbot, S. (2019). Slow-slip, slow earthquakes, period-two cycles, full and partial
491 ruptures, and deterministic chaos in a single asperity fault. *Tectonophysics*, *768*,
492 228171.
- 493 Baumann, C., & Dalguer, L. A. (2014). Evaluating the compatibility of dynamic
494 rupture-based synthetic ground motion with empirical ground-motion prediction
495 equation. *Bulletin of the Seismological Society of America*, *104*(2), 634–652.
- 496 Ben-Menahem, A., & Harkrider, D. G. (1964). Radiation patterns of seismic surface
497 waves from buried dipolar point sources in a flat stratified earth. *Journal of Geo-*
498 *physical Research*, *69*(12), 2605–2620.
- 499 Boore, D. M., Watson-Lamprey, J., & Abrahamson, N. A. (2006). Orientation-
500 independent measures of ground motion. *Bulletin of the seismological Society of*
501 *America*, *96*(4A), 1502–1511.
- 502 Brune, J. N. (1970). Tectonic stress and the spectra of seismic shear waves from
503 earthquakes. *Journal of geophysical research*, *75*(26), 4997–5009.
- 504 Bydlon, S. A., Withers, K. B., & Dunham, E. M. (2019). Combining Dynamic Rup-
505 ture Simulations with Ground-Motion Data to Characterize Seismic Hazard from
506 M w 3 to 5.8 Earthquakes in Oklahoma and Kansas. *Bulletin of the Seismological*
507 *Society of America*, *109*(2), 652–671.
- 508 Cattania, C. (2019). Complex earthquake sequences on simple faults. *Geophysical*
509 *Research Letters*, *46*(17-18), 10384–10393.
- 510 Cochran, E. S., Li, Y.-G., Shearer, P. M., Barbot, S., Fialko, Y., & Vidale, J. E.
511 (2009). Seismic and geodetic evidence for extensive, long-lived fault damage zones.
512 *Geology*, *37*(4), 315–318.
- 513 Cotton, F., Archuleta, R., & Causse, M. (2013). What is sigma of the stress drop?
514 *Seismological Research Letters*, *84*(1), 42–48.
- 515 Courboux, F., Dujardin, A., Vallée, M., Delouis, B., Sira, C., Deschamps, A., ...
516 Thouvenot, F. (2013). High-frequency directivity effect for an M w 4.1 earth-
517 quake, widely felt by the population in southeastern France. *Bulletin of the*
518 *Seismological Society of America*, *103*(6), 3347–3353.
- 519 Crempien, J. G., & Archuleta, R. J. (2018). Within-event and between-events
520 ground motion variability from earthquake rupture scenarios. In *Best practices*
521 *in physics-based fault rupture models for seismic hazard assessment of nuclear*
522 *installations* (pp. 127–141). Springer.
- 523 Das, S., & Aki, K. (1977). Fault plane with barriers: A versatile earthquake model.
524 *Journal of geophysical research*, *82*(36), 5658–5670.
- 525 Dunham, E. M., & Bhat, H. S. (2008). Attenuation of radiated ground motion and

- stresses from three-dimensional supershear ruptures. *Journal of Geophysical Research: Solid Earth*, 113(B8).
- Field, E. H., Arrowsmith, R. J., Biasi, G. P., Bird, P., Dawson, T. E., Felzer, K. R., ... others (2014). Uniform California earthquake rupture forecast, version 3 (UCERF3)—The time-independent model. *Bulletin of the Seismological Society of America*, 104(3), 1122–1180.
- Gabriel, A.-A., Ampuero, J.-P., Dalguer, L., & Mai, P. M. (2013). Source properties of dynamic rupture pulses with off-fault plasticity. *Journal of Geophysical Research: Solid Earth*, 118(8), 4117–4126.
- Galvez, P., Ampuero, J.-P., Dalguer, L. A., Somala, S. N., & Nissen-Meyer, T. (2014). Dynamic earthquake rupture modelled with an unstructured 3-D spectral element method applied to the 2011 M 9 Tohoku earthquake. *Geophysical Journal International*, 198(2), 1222–1240.
- Geist, E. L., Oglesby, D., & Ryan, K. (2019). Tsunamis: Stochastic models of generation, propagation, and occurrence.
- Griffith, A. A. (1921). VI. The phenomena of rupture and flow in solids. *Philosophical transactions of the royal society of london. Series A, containing papers of a mathematical or physical character*, 221(582-593), 163–198.
- Gutteri, M., & Spudich, P. (2000). What can strong-motion data tell us about slip-weakening fault-friction laws? *Bulletin of the Seismological Society of America*, 90(1), 98–116.
- Harris, R. A. (2004). Numerical simulations of large earthquakes: Dynamic rupture propagation on heterogeneous faults. In *Computational earthquake science part ii* (pp. 2171–2181). Springer.
- Hauksson, E., & Meier, M.-A. (2019). Applying depth distribution of seismicity to determine thermo-mechanical properties of the seismogenic crust in Southern California: comparing lithotectonic blocks. *Pure and Applied Geophysics*, 176(3), 1061–1081.
- Huang, Y. (2021). Smooth Crustal Velocity Models Cause a Depletion of High-Frequency Ground Motions on Soil in 2D Dynamic Rupture Simulations. *Bulletin of the Seismological Society of America*, 111(4), 2057–2070.
- Huang, Y., Ampuero, J.-P., & Helmberger, D. V. (2016). The potential for supershear earthquakes in damaged fault zones—theory and observations. *Earth and Planetary Science Letters*, 433, 109–115.
- Hutton, K., Woessner, J., & Hauksson, E. (2010). Earthquake monitoring in southern California for seventy-seven years (1932–2008). *Bulletin of the Seismological Society of America*, 100(2), 423–446.
- Ide, S., & Takeo, M. (1997). Determination of constitutive relations of fault slip based on seismic wave analysis. *Journal of Geophysical Research: Solid Earth*, 102(B12), 27379–27391.
- Ji, C., & Archuleta, R. J. (2021). Two empirical double-corner-frequency source spectra and their physical implications. *Bulletin of the Seismological Society of America*, 111(2), 737–761.
- Kanamori, H., & Anderson, D. L. (1975). Theoretical basis of some empirical relations in seismology. *Bulletin of the seismological society of America*, 65(5), 1073–1095.
- Kaneko, Y., Lapusta, N., & Ampuero, J.-P. (2008). Spectral element modeling of spontaneous earthquake rupture on rate and state faults: Effect of velocity-strengthening friction at shallow depths. *Journal of Geophysical Research: Solid Earth*, 113(B9).
- Keilis-Borok, V., & Monin, A. (1959). Magnetoelastic waves and the boundary of the earth's core. *Izv. Akad. Nauk SSSR, Ser. Geofiz*(11), 1529–1541.
- Lavallée, D., & Archuleta, R. J. (2003). Stochastic modeling of slip spatial complexities for the 1979 Imperial Valley, California, earthquake. *Geophysical Research*

- 580 *Letters*, 30(5).
- 581 Lavallée, D., Liu, P., & Archuleta, R. J. (2006). Stochastic model of heterogeneity
582 in earthquake slip spatial distributions. *Geophysical Journal International*, 165(2),
583 622–640.
- 584 Lewis, M. A., & Ben-Zion, Y. (2010). Diversity of fault zone damage and trapping
585 structures in the Parkfield section of the San Andreas Fault from comprehensive
586 analysis of near fault seismograms. *Geophysical Journal International*, 183(3),
587 1579–1595.
- 588 Liu, D., & Duan, B. (2018). Scenario earthquake and ground-motion simulations
589 in North China: Effects of heterogeneous fault stress and 3D basin structure. *Bul-*
590 *letin of the Seismological Society of America*, 108(4), 2148–2169.
- 591 Lozos, J. C., Oglesby, D. D., Brune, J. N., & Olsen, K. B. (2015). Rupture and
592 ground-motion models on the northern San Jacinto fault, incorporating realistic
593 complexity. *Bulletin of the Seismological Society of America*, 105(4), 1931–1946.
- 594 Mai, P. M., & Beroza, G. C. (2002). A spatial random field model to character-
595 ize complexity in earthquake slip. *Journal of Geophysical Research: Solid Earth*,
596 107(B11), ESE–10.
- 597 Manighetti, I., Caulet, C., De Barros, L., Perrin, C., Cappa, F., & Gaudemer, Y.
598 (2015). Generic along-strike segmentation of African normal faults, East Africa:
599 Implications on fault growth and stress heterogeneity on seismogenic fault planes.
600 *Geochemistry, Geophysics, Geosystems*, 16(2), 443–467.
- 601 Mena, B., Dalguer, L., & Mai, P. M. (2012). Pseudodynamic source characterization
602 for strike-slip faulting including stress heterogeneity and super-shear ruptures.
603 *Bulletin of the Seismological Society of America*, 102(4), 1654–1680.
- 604 Milliner, C. W. D., Dolan, J. F., Hollingsworth, J., Leprince, S., Ayoub, F., & Sam-
605 mis, C. G. (2015). Quantifying near-field and off-fault deformation patterns of the
606 1992 Mw 7.3 Landers earthquake. *Geochemistry, Geophysics, Geosystems*, 16(5),
607 1577–1598.
- 608 Nielsen, S. B., & Olsen, K. B. (2000). Constraints on stress and friction from
609 dynamic rupture models of the 1994 Northridge, California, earthquake. In *Micro-*
610 *scopic and macroscopic simulation: Towards predictive modelling of the earthquake*
611 *process* (pp. 2029–2046). Springer.
- 612 Oglesby, D. D., & Day, S. M. (2002). Stochastic fault stress: Implications for fault
613 dynamics and ground motion. *Bulletin of the Seismological Society of America*,
614 92(8), 3006–3021.
- 615 Oral, E., Weng, H., & Ampuero, J. P. (2020). Does a damaged-fault zone mit-
616 igate the near-field impact of supershear earthquakes?—Application to the
617 2018 7.5 Palu, Indonesia, earthquake. *Geophysical Research Letters*, 47(1),
618 e2019GL085649.
- 619 Ozacar, A. A., & Beck, S. L. (2004). The 2002 Denali fault and 2001 Kunlun fault
620 earthquakes: complex rupture processes of two large strike-slip events. *Bulletin of*
621 *the Seismological Society of America*, 94(6B), S278–S292.
- 622 Page, M., & Felzer, K. (2015). Southern San Andreas fault seismicity is consistent
623 with the Gutenberg–Richter magnitude–frequency distribution. *Bulletin of the*
624 *Seismological Society of America*, 105(4), 2070–2080.
- 625 Powers, P. M., & Jordan, T. H. (2010). Distribution of seismicity across strike-slip
626 faults in California. *Journal of Geophysical Research: Solid Earth*, 115(B5).
- 627 Prada, M., Galvez, P., Ampuero, J.-P., Sallarès, V., Sánchez-Linares, C., Macías,
628 J., & Peter, D. (2021). The Influence of Depth-Varying Elastic Properties of the
629 Upper Plate on Megathrust Earthquake Rupture Dynamics and Tsunamigenesis.
630 *Journal of Geophysical Research: Solid Earth*, 126(11), e2021JB022328.
- 631 Qiu, H., Ben-Zion, Y., Catchings, R., Goldman, M. R., Allam, A. A., & Steidl, J.
632 (2021). Seismic imaging of the Mw 7.1 Ridgecrest earthquake rupture zone from
633 data recorded by dense linear arrays. *Journal of Geophysical Research: Solid*

- 634 *Earth*, 126(7), e2021JB022043.
- 635 Ripperger, J., Ampuero, J.-P., Mai, P., & Giardini, D. (2007). Earthquake source
636 characteristics from dynamic rupture with constrained stochastic fault stress.
637 *Journal of Geophysical Research: Solid Earth*, 112(B4).
- 638 Ripperger, J., Mai, P., & Ampuero, J.-P. (2008). Variability of near-field ground
639 motion from dynamic earthquake rupture simulations. *Bulletin of the seismological*
640 *society of America*, 98(3), 1207–1228.
- 641 Rodriguez Padilla, A. M., Oskin, M. E., Milliner, C. W., & Plesch, A. (2022). Ac-
642 cretal of widespread rock damage from the 2019 Ridgecrest earthquakes. *Nature*
643 *Geoscience*, 1–5.
- 644 Ruiz, J., Ampuero, J. P., & Mai, P. M. (2008). *Validation of source dynamic mod-*
645 *els for GMP: sufficient requirements on fault heterogeneities - A collaborative*
646 *proposal, Award Number 08039.*
- 647 Sato, R. (1972). Stress drop for a finite fault. *Journal of Physics of the Earth*,
648 20(4), 397–407.
- 649 SCEDC. (2013). Southern California Earthquake Data Center. Caltech. Dataset.
- 650 Shebalin, P., & Narteau, C. (2017). Depth dependent stress revealed by aftershocks.
651 *Nature communications*, 8(1), 1–8.
- 652 Singh, S. K. (1977). Slip and stress drop on a circular fault. *Bulletin of the Seismo-*
653 *logical Society of America*, 67(2), 279–284.
- 654 Somerville, P. G., Smith, N. F., Graves, R. W., & Abrahamson, N. A. (1997).
655 Modification of empirical strong ground motion attenuation relations to include
656 the amplitude and duration effects of rupture directivity. *Seismological research*
657 *letters*, 68(1), 199–222.
- 658 Tormann, T., Wiemer, S., & Hauksson, E. (2010). Changes of reporting rates in
659 the southern California earthquake catalog, introduced by a new definition of ML.
660 *Bulletin of the Seismological Society of America*, 100(4), 1733–1742.
- 661 Tromp, J., Komatitsch, D., & Liu, Q. (2008). Spectral-element and adjoint methods
662 in seismology. *Communications in Computational Physics*, 3(1), 1–32.
- 663 Wells, D. L., & Coppersmith, K. J. (1994). New empirical relationships among
664 magnitude, rupture length, rupture width, rupture area, and surface displacement.
665 *Bulletin of the seismological Society of America*, 84(4), 974–1002.
- 666 White, M. C., Fang, H., Catchings, R. D., Goldman, M. R., Steidl, J. H., & Ben-
667 Zion, Y. (2021). Detailed traveltimes tomography and seismic catalogue around
668 the 2019 M w7. 1 Ridgecrest, California, earthquake using dense rapid-response
669 seismic data. *Geophysical Journal International*, 227(1), 204–227.
- 670 Withers, K. B., Ma, S., Wang, Y., Ulrich, T., Liu, D., Duan, B., . . . Asimaki, D.
671 (2021). *Generation of Broadband Ground Motion from Dynamic Rupture Simula-*
672 *tions: A Group Modeling Approach towards better Characterizing Seismic Hazard*
673 *for Engineering Applications.* SCEC Contribution 11344.
- 674 Yang, Y., Atterholt, J. W., Shen, Z., Muir, J. B., Williams, E. F., & Zhan, Z.
675 (2022). Sub-kilometer correlation between near-surface structure and ground
676 motion measured with distributed acoustic sensing. *Geophysical Research Letters*,
677 e2021GL096503.

678 **Full mailing addresses**

679 **Elif Oral ^{1,2}, Jean Paul Ampuero ¹, Javier Ruiz ³, Domniki Asimaki ²**

680 ¹Université Côte d'Azur, IRD, CNRS, Observatoire de la Côte d'Azur, Géoazur, 250 Rue Albert Einstein,
681 06560 Valbonne, France

682 ²Mechanical and Civil Engineering, California Institute of Technology, 1200 E California Blvd, Pasadena,
683 CA 91125

684 ³Universidad de Chile, Departamento de Geofísica, FCFM, Av. Alameda 2002, Santiago,
685 Región Metropolitana, Chile

686 **Tables**

Table 1: Properties of the three heterogeneous models: range of magnitudes and rupture radii of the past seismicity, and hypocenter location of the target earthquake.

Model	M_w	Radius (km)	Hypocenter (km, km)
I	4.75-6.5	1.35-10.11	(1.45, -7.0)
II	4.75-6.5	1.35-10.11	(-2.70, -5.4)
III	3.5-6.5	0.32-10.11	(1, -7)

Table 2: Rupture properties of the three heterogeneous models.

Model	M_w	Ave. stress drop (MPa)	Surface rupture (km)
I	7.00	2.7	49.7
II	7.05	2.7	52.8
III	7.12	2.9	63.5

List of Figure Captions

Figure 1: Past seismicity of the San Jacinto fault, southern California. (a) Map view of the fault (black line) and regional seismicity (circles). Selected events within 10 km of the fault are shown as black circles and contoured by black line. b) Spatial distribution of past earthquakes within a distance of 10 km to the fault trace, projected on the fault plane. The minimum magnitude of the catalog is 3.5, and the date of the oldest event is 1960-04-21. Circles indicate rupture areas assuming circular ruptures with uniform stress drop of 3 MPa. Darker circles correspond to more recent events. (c) Magnitude distribution of the selected events. The dashed and solid lines indicate number-magnitude distributions with $b = 0.95$, for maximum magnitudes of 6 (as in the selected seismicity) and 7 (the target of this study), respectively.

Figure 2: Example of preparation of initial stress heterogeneity. (a) Number-magnitude distribution, (b) seismicity by depth of the example model, (c) reference seismicity by depth, (d) spatial distribution of past events, (e) shear stress ratio along strike, (f) same as (e) for along dip direction.

Figure 3: Three models of stress heterogeneity. Number-magnitude distribution (top left), seismicity by depth (top right), and shear stress ratio along strike (bottom) for (a) Model I, (b) Model II, and (c) Model III.

Figure 4: Comparison of Model I synthetics with GMPEs. Spectral acceleration at periods of 0.5 (left), 1 (middle), and 3 (right) seconds. Mean values of synthetics are shown by scatter plot, and standard variation is indicated by the vertical bars. GMPE mean (solid line) and mean \pm one standard deviation (dashed lines) are shown in black.

Figure 5: Snapshots of rupture propagation. Variation of slip at different instants shown for Model I (a), Model II (b), and Model III (c).

Figure 6: Source spectra. Comparison of moment rate spectra between the three heterogeneous models, the empirical model of Ji & Archuleta (2021) denoted by JA19_2S, and the ω^{-2} model for magnitude 7.

Figure 7: Ground motion and source properties of Model I. Top: amplitude and polarization of peak ground velocity near the fault. The dominant polarization is either fault-parallel (FP) or fault-normal (FN). The epicenter position is indicated by a vertical dashed line. Middle: stress drop. Bottom: rupture speed. The hypocenter location is indicated by a star. Rupture extent is indicated by a solid white line.

Figure 8: Ground motion comparison between homogeneous and heterogeneous stress models. Spatial distribution of PGV amplitude for (a) the homogeneous model without medium stratification and (b) Model I. Spatial distribution of PGV polarization for (c) the same homogeneous model and (d) Model I. Surface rupture extension is shown by solid lines. FP and FN stand for fault-parallel and fault-normal, respectively.

Figure 9: Site effect on source spectra. Comparison of moment rate spectra between two homogeneous models, with and without stratification: the empirical model of Ji & Archuleta (2021) denoted by JA19_2S, and the ω^{-2} model.

Figures

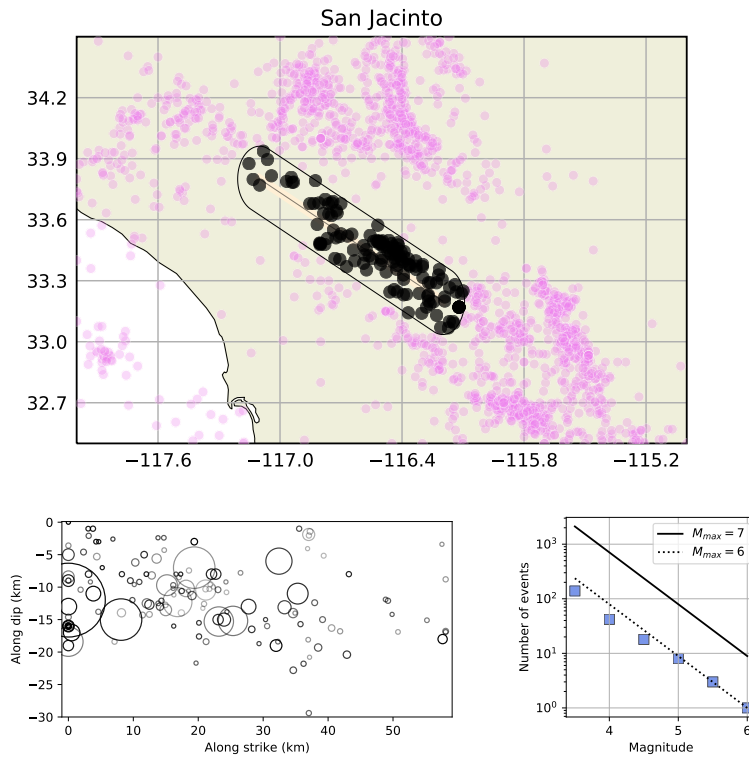


Figure 1: Past seismicity of the San Jacinto fault, southern California. (a) Map view of the fault (black line) and regional seismicity (circles). Selected events within 10 km of the fault are shown as black circles and contoured by black line. b) Spatial distribution of past earthquakes within a distance of 10 km to the fault trace, projected on the fault plane. The minimum magnitude of the catalog is 3.5, and the date of the oldest event is 1960-04-21. Circles indicate rupture areas assuming circular ruptures with uniform stress drop of 3 MPa. Darker circles correspond to more recent events. (c) Magnitude distribution of the selected events. The dashed and solid lines indicate number-magnitude distributions with $b = 0.95$, for maximum magnitudes of 6 (as in the selected seismicity) and 7 (the target of this study), respectively.

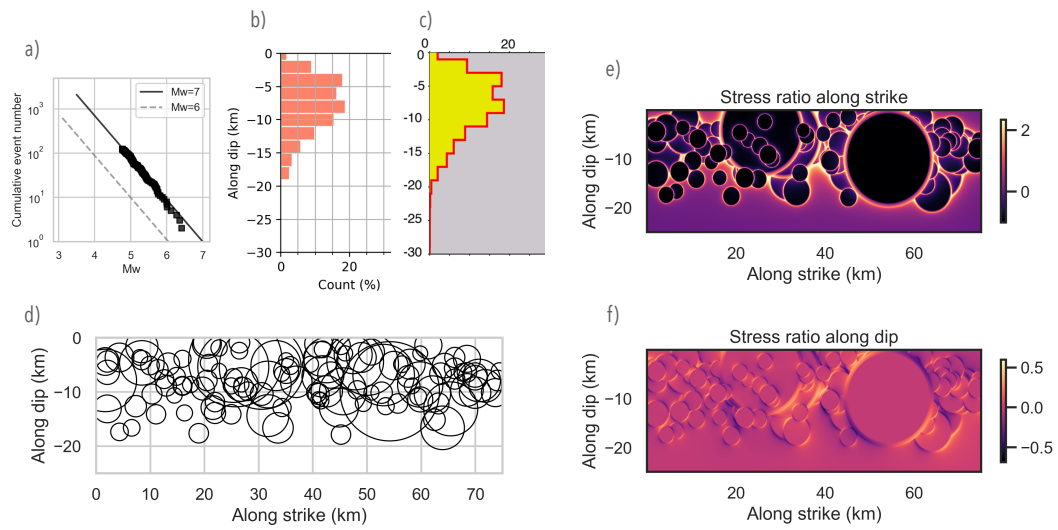


Figure 2: Example of preparation of initial stress heterogeneity. (a) Number-magnitude distribution, (b) seismicity by depth of the example model, (c) reference seismicity by depth, (d) spatial distribution of past events, (e) shear stress ratio along strike, (f) same as (e) for along dip direction.

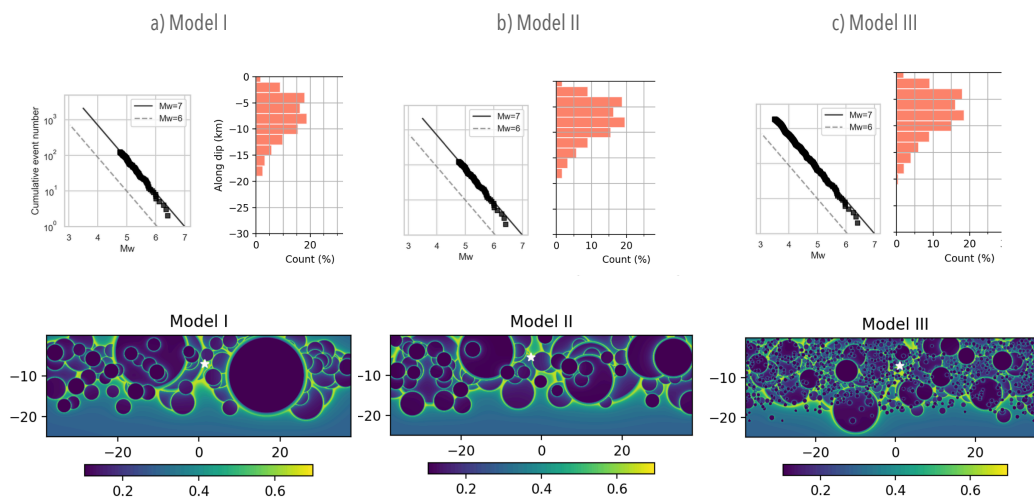


Figure 3: Three models of stress heterogeneity. Number-magnitude distribution (top left), seismicity by depth (top right), and shear stress ratio along strike (bottom) for (a) Model I, (b) Model II, and (c) Model III.

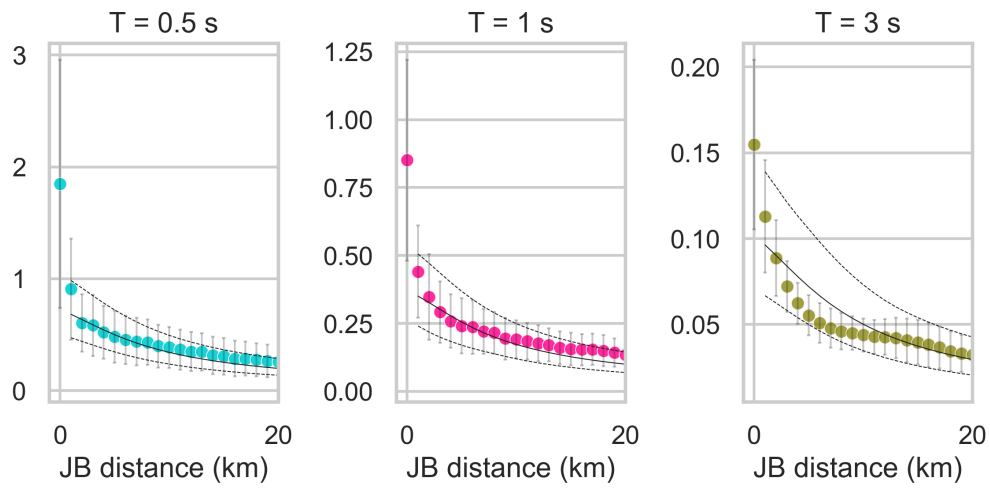


Figure 4: Comparison of Model I synthetics with GMPEs. Spectral acceleration at periods of 0.5 (left), 1 (middle), and 3 (right) seconds. Mean values of synthetics are shown by scatter plot, and standard variation is indicated by the vertical bars. GMPE mean (solid line) and mean \pm one standard deviation (dashed lines) are shown in black.

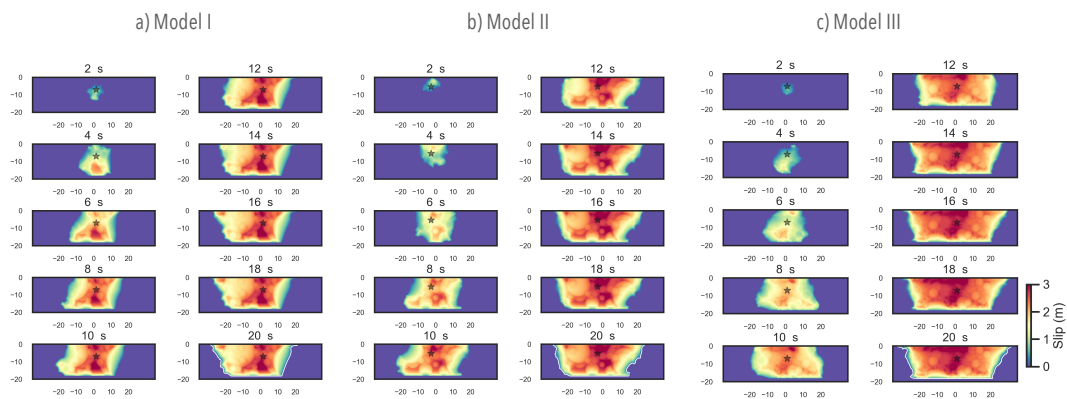


Figure 5: Snapshots of rupture propagation. Variation of slip at different instants shown for Model I (a), Model II (b), and Model III (c).

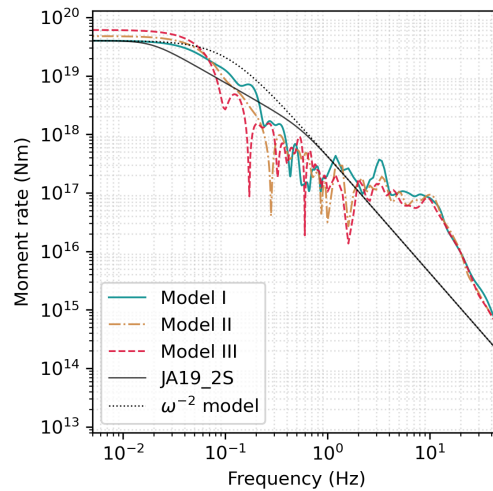


Figure 6: Source spectra. Comparison of moment rate spectra between the three heterogeneous models, the empirical model of Ji & Archuleta (2021) denoted by JA19_2S, and the ω^{-2} model for magnitude 7.

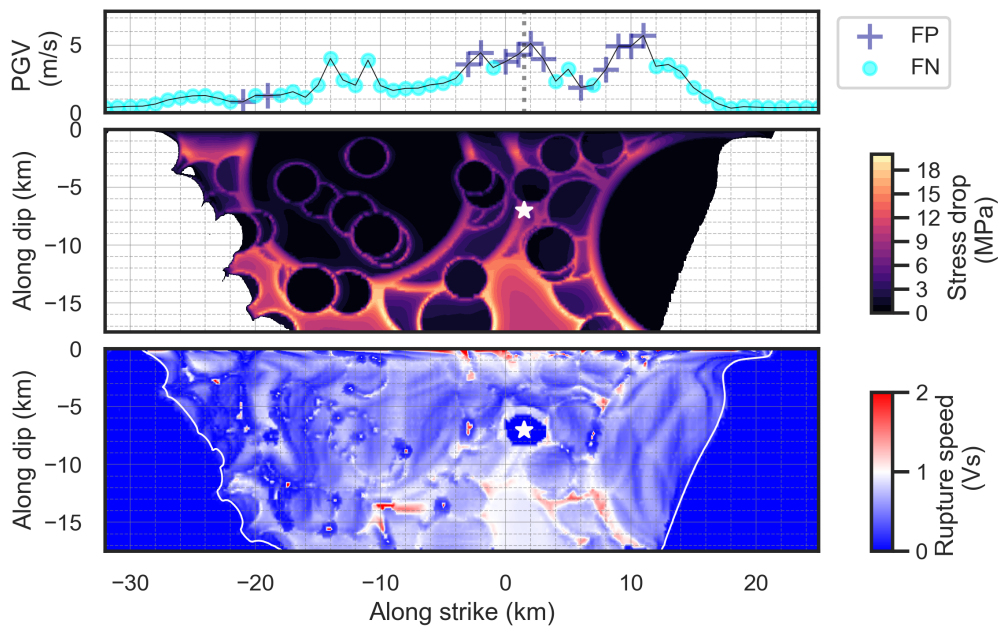


Figure 7: Ground motion and source properties of Model I. Top: amplitude and polarization of peak ground velocity near the fault. The dominant polarization is either fault-parallel (FP) or fault-normal (FN). The epicenter position is indicated by a vertical dashed line. Middle: stress drop. Bottom: rupture speed. The hypocenter location is indicated by a star. Rupture extent is indicated by a solid white line.

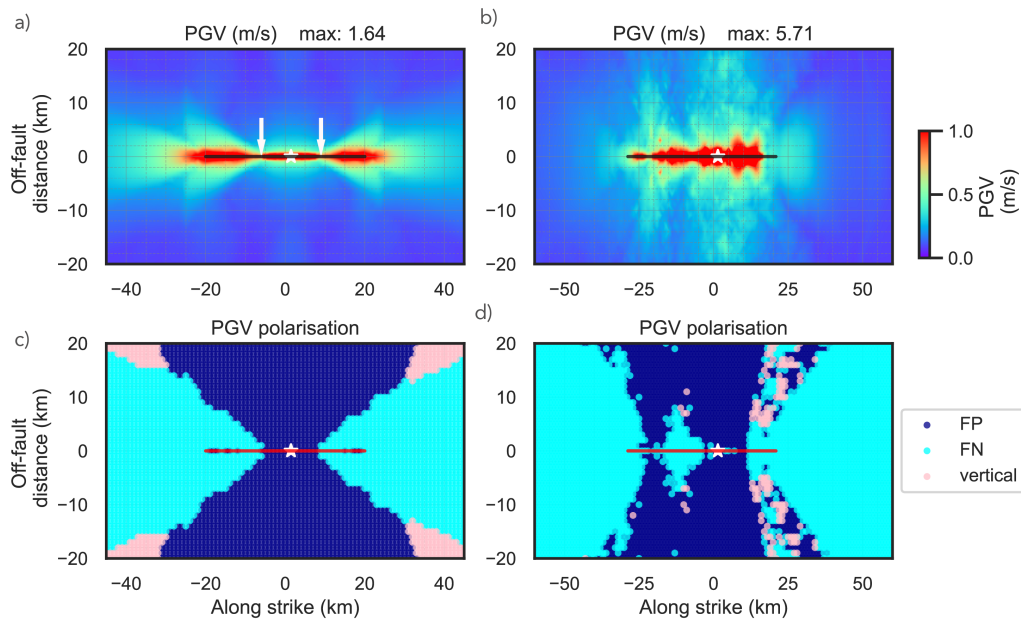


Figure 8: Ground motion comparison between homogeneous and heterogeneous stress models. Spatial distribution of PGV amplitude for (a) the homogeneous model without medium stratification and (b) Model I. Spatial distribution of PGV polarization for (c) the same homogeneous model and (d) Model I. Surface rupture extension is shown by solid lines. FP and FN stand for fault-parallel and fault-normal, respectively.

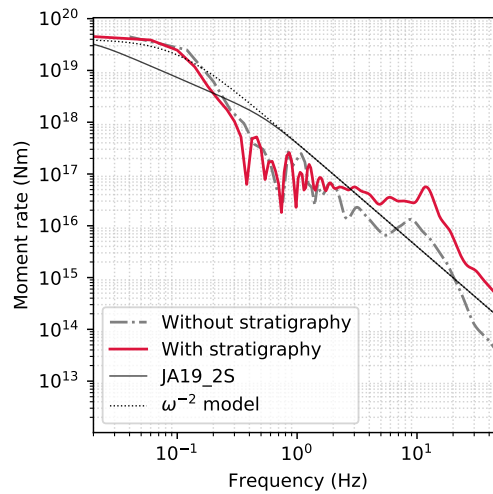


Figure 9: Site effect on source spectra. Comparison of moment rate spectra between two homogeneous models, with and without stratification: the empirical spectra of Ji & Archuleta (2021) denoted by JA19_2S, and the ω^{-2} model.

689 **Appendix A Stress change induced by each background earthquake**

We treat each past earthquake as a circular rupture with uniform stress drop. The slip Δu at a distance $r < a$ from the center of a rupture of radius a is (Keilis-Borok & Monin, 1959):

$$\Delta u(r) = u_{max}(1 - r^2/a^2)^{1/2} \tag{A1}$$

690 where u_{max} is the maximum slip.

691 The stress change on the fault at $(x, y) = (r \cos \alpha, r \sin \alpha)$ is (Sato, 1972; Singh, 1977):

$$\Delta \sigma = 1/2 \cdot (\pi \cdot a/2)^{1/2} \mu u_{max} [K_0 I_0(r/a) - K_1 \cos(2\alpha) I_2(r/a)] \tag{A2}$$

693 where $K_0 = \gamma + 1/2$, $K_1 = \gamma - 1/2$, $\gamma = (\lambda + \mu)/(\lambda + 2\mu)$, λ and μ are Lamé constants, 694 I_0 and I_2 are integrals provided by Singh (1977) for all values of r/a .

695 The integrals are singular at $r = a$. To avoid this singularity, we convolve the shear 696 stresses with a unitary area boxcar function of width da . The convolution integral is ap- 697 plied along the r variable. The resulting regularized shear stresses used in the numer- 698 ical computation are:

$$\tau_{12} = -C \begin{cases} K_0 \frac{1}{a} \left(\frac{\pi}{2a}\right)^{1/2} & r < a \\ K_0 \frac{1}{a} \left(\frac{\pi}{2a}\right)^{1/2} \frac{[a-r+da]}{da} + \frac{[f(r)-f(a)]}{da} & a \leq r < a + da \\ \frac{[f(r)-f(r-da)]}{da} & r \geq a + da \end{cases} \tag{A3}$$

$$\tau_{23} = -C \begin{cases} 0 & r < a \\ K_1 \left(\frac{2a}{\pi}\right)^{1/2} \sin(2\alpha) \left\{ I_2(r) - I_2(a) \right\} \frac{1}{da} & a \leq r < a + da \\ K_1 \left(\frac{2a}{\pi}\right)^{1/2} \sin(2\alpha) \left\{ I_2(r) - I_2(r - da) \right\} \frac{1}{da} & r \geq a + da \end{cases} \tag{A4}$$

699 where τ_{12} and τ_{23} are shear stress along strike and dip, respectively; C scalar and the 700 functions $I_1(r)$, $I_2(r)$, and $f(r)$ are set as follows:

$$C = \frac{1}{2} \left(\frac{\pi a}{2}\right)^{1/2} \mu u_{max} \tag{A5}$$

$$f(r) = K_0 \frac{-1}{a} \left(\frac{2}{\pi a}\right)^{1/2} I_1(r) - K_1 \left(\frac{2a}{\pi}\right)^{1/2} \cos(2\alpha) I_2(r) \tag{A6}$$

$$I_2(r) = \frac{\sqrt{r^2 - a^2}}{ar} \tag{A7}$$

$$I_1(r) = -r \arctan \left(\frac{a}{\sqrt{r^2 - a^2}} \right) \tag{A8}$$

After calculating the stress changes for a past event, we scale the stress values by a factor $rscal$ to set the maximum stress change equal to a cut-off value, τ_{max} :

$$rscal = (\tau_{max}/max(\tau_{12}) - 1)(\tau_{12} + \mu)/(max(\tau_{12}) + \mu) \tag{A9}$$

701 We set $\tau_{max} = \mu S$ where $S = (\mu_s - \mu_b)/(\mu_b - \mu_d)$. Here, $S = 2.33$ ($\mu_s = 0.7$, $\mu_d = 0.1$ 702 and $\mu_b = 0.28$).

703 After each event, we set the cumulative stress equal to τ_{12} and τ_{23} inside its rup-
 704 ture. Outside the rupture, we add the changes τ_{12} and τ_{23} to the pre-existing shear stresses
 705 and set the upper limit for τ_{12} as τ_{max} .

706 **Appendix B Adjusting stress ratios to the 3D model**

The procedure in Appendix A is based on the assumption of a spatially uniform medium. We adjust the shear stresses to our depth-dependent model, such that we derive stress ratios $r_{12,23} = \tau_{12,23}/\mu$. We determine the initial stresses, τ_0 , at each point of the fault grid in the 3D mesh by the following equation, such that the maximum stress equals the static strength, $\mu_s\sigma'$:

$$\tau_{0;12,23} = \sigma' \cdot [\mu_b + r_{12,23}(\mu_b - \mu_d)] \quad (\text{B1})$$

707 where σ' is the effective stress. We set the upper limit of shear stress slightly below the
 708 static strength as $max(\tau) = \tau_s - 0.1(\tau_s - \tau_d)$, where τ_s and $\tau_d = \mu_d\sigma'$ are static and
 709 dynamic shear strength, respectively. We do this by cutting down the values that exceed
 710 this threshold.